RESERVOIR CHARACTERIZATION WITH PORE NETWORK EXTRACTION APPLIED TO PRESALT ANALOG SAMPLE

Daniel M. Plucenio

Edson T. M. Manoel

Leonardo P. Rangel

Eduardo Kern

Rafael F. Bertoldi

Martin Prusse

dplucenio@esss.com.br

edson.tadeu@esss.com.br

leonardo.rangel@esss.com.br

kern@esss.com.br

bertoldi@esss.com.br

prusse@esss.com.br

ESSS (Engineering Simulation & Scientific Software)

Rua Orlando Phillipi, nº100, Edifício Techplan, 1º andar, Saco Grande, CEP: 88032-700, Florianópolis, SC, Brasil

Leonardo Verbicaro Perdomo

Jaqueline Saad

leonardo.verbicaro@concremat.com.br

jaqueline.saad@concremat.com.br

Concremat

Rua Euclides da Cunha nº 106, São Cristóvão, CEP: 20940-060, Rio de Janeiro - RJ- Brasil

Webster Mohriak

webmohr@gmail.com

Universidade do Estado do Rio de Janeiro

Rua São Francisco Xavier, 524, Maracanã, CEP: 20550-900, Rio de Janeiro - RJ - Brasil

Abstract. *Methods based on image analysis are proving to be a powerful ally for reservoir rock characterization. Once a three-dimensional image is obtained, petrophysical properties can be estimated using a mathematical model that captures the physics of fluid flow through porous media. This work uses the Pore network extraction methodology. Fluid flow is simulated by treating the network as a hydraulic system. Shape factors are used to capture the flow resistance of the original porous structures. A system of equations is composed using generalized Poiseulle's equation in order to find pressure values for each pore. The main advantage of this methodology is the capability of analyzing larger images, which are becoming increasingly necessary in the characterization of carbonate rocks, whose computational costs required by other existing methods are very high and often prohibitive. Pore networks generated from siliciclastic rock images are shown as well as the results obtained with the model for absolute permeability and porosity which are compared with experimental data. Networks and results generated from carbonate rock similar to those found in Pre-salt reservoirs are presented and challenges of carbonate characterization with image analysis is discussed*

Keywords: *Pore Network, Image analysys, Digital rock, Reservoir characterization*

1 INTRODUCTION

Experimental methods are still the most trusted and accepted approach used by the oil and gas industry in order to obtain reservoirs petrophysical properties. These experiments are mostly performed on core samples extracted from reservoir rocks of interest.

These experiments are, however, often expensive and time demanding. In the search for viable alternatives, property estimation through image analysis is proving to be an useful tool for preliminary analysis and capable of complementing some of the experiments. This family of methods has the folowing advantages (Cunha, et al., 2012):

- Consistency and repeatability of the analyzes;
- Reduction of costs and execution time compared to experimental methods;
- Acquirement of parameters that can only be directly obtained through images, such as connectivity of the porous structure and geometry of the pores and grains;
- Extraction of various petrophysical properties from the same sample.

In general, some of the steps that may be used to employ such techniques can be listed as:

1. Extraction of three-dimensional image of the sample;
2. Image segmentation and binarization;
3. Calculation of petrophysical property.

The next section describes image acquisition using X-Ray computed microtomography, which was the method used in this work.

1.1 X-Ray computed tomography

In 1895, German physicist Wilhelm Röntgen discovered a new type of radiation while studying luminescent phenomena. Known as X-rays, it had particular characteristics: it did not ionize the air, it was not affected by electrical and electromagnetic fields and it could pass through solid materials. It is now known that these are electromagnetic emissions with short wavelength (0.05 ångström up to dozens of ångström) (Mantovani, 2013).

While going through a given material, the radiation attenuates its intensity due to scattering and absorption processes. This attenuation can be described by the Beer-Lambert equation:

$$\begin{aligned} I &= I_0 e^{-\lambda x} \\ I_0 &= I(x=0) \end{aligned} \quad (1)$$

Where x is the sample thickness, I_0 is the intensity inciding on the sample, I is the resulting intensity after the passage and λ is the linear attenuation coefficient. This ratio depends on the molecular weight and the density of the material. The tomography X-ray aims to map this attenuation coefficient, which will infer the density variations of the material being analyzed. In X-ray computed tomography (CT), instead of one, several projections are taken while the sample is rotated in small angles. The three-dimensional image is then constructed from the various two-dimensional projections using numerical processing

CT scanners have evolved in such a way that today spatial resolution reaches nanoscale, therefore making CT a great method to obtain three-dimensional images of the porous medium. It has the benefit of being a non-destructive method, using "direct imaging" (direct extraction of the sample data).

1.2 Binarization

The rock sample image extracted using CT presents a distribution density of the material, generally represented by grayscale voxels. It is necessary, however, to define which one of these are grain and which are pore voxels. It is usual to represent each voxel with the value of 0 or 1, and this process is called binarization.

Binarization involves comparing the density of each voxel image with a certain threshold or limit, so that if the density is above this threshold, it assumes the value of 1 and otherwise, takes the value of 0.

The threshold value may be the same for all voxels (global) or may vary across the image (local). The choice of the threshold value can be performed manually or through a numerical analysis, from which one can choose from many existing algorithms (Sezgin et. al, 2004, as cited in Silva et al, 2012) whose details are beyond the scope of this work.

1.3 Petrophysical properties prediction

Petrophysical properties of the rock sample, such as such as absolute permeability, relative permeability and capillary pressure, can be calculated from the representation of the porous three-dimensional domain in a binarized image. These properties are estimated using fluid flow numerical simulation. Currently, two major approaches are considered regarding the simulation of flow in porous structures: Lattice Boltzmann method and methods based on Pore-network concept.

Lattice Boltzmann methods use a simplified model of particle simulation capturing the essential physics at the microscopic or mesoscopic scale so that the average properties of the simplified model meet the macroscopic equations. The method is a good approximation of the Navier-Stokes equation and is used in simulations with complex boundary conditions and multiphase flows interfaces (Rothman & Zaleski, 1994) (Chen & Doolen, 1998), (Benzi, et al., 1992) cited in (Al-Kharusi & Blunt, 2008).

The application of Lattice Boltzmann modeling is well accepted in the industry but is limited by its high computational costs (Chen & Doolen, 1998), being prohibitive in some situations, especially when we are thinking about extending the technique for analysis of a rock with multiple resolution scales.

1.4 Pore-network method

The approach alternative to Lattice Boltzmann is the Pore-network method, which works by constructing a structure that is topologically equivalent to the porous system obtained in the image (i.e., preserving the connectivity between the pores) but with a simplified geometry.

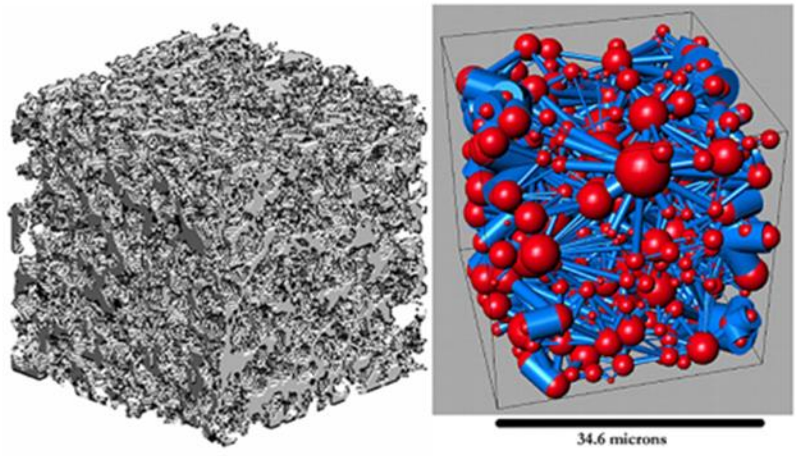

Figure 1 Pore-network extracted by Øren (2002), (2003)

The network mimics the porous rock in its nature, which is composed of larger spaces between grains (called pores) and elongated openings (throats or connections) that connect these spaces. It is assumed that both pores and throats have constant cross sections, with shape factors being applied to represent tortuosity and irregularities of the actual structures. Once this network is determined, the flow can be calculated through a semi-analytic method where pores act as fluid storage and throats act as fluid flow channels between one pore to another.

2 PORE-NETWORK EXTRACTION

In this section the concepts and steps involved in network extraction process of pores and throats from a binarized image will be presented in detail

Among the existing methods presented in literature for pore-network extraction, the maximal balls method was chosen. The motivation is that, according to literature, this method provides a good representation of porous media and good capacity for identification and differentiation of pores and throats. It is also referenced as a versatile and robust method when compared to the median axis methods whose results and network representativeness are highly dependent on existing noise from the acquired image. Networks extractions based on medial-axis method define pores as the merge of two medial-axis branches. This can be observed for example in Figure 2 where a medial-axis extraction method would segment the porous space in four different pores, whereas with maximal spheres method the figure would be classified as one single pore. Medial-axis algorithm need a further post-processing step in order to trim the skeleton and fuse the junctions together to avoid overestimated coordination numbers.

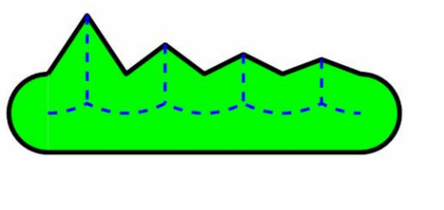

Figure 2 Porous structure representation showing its medial-axis skeleton

The methodology used for network extraction is based on maximal balls concept. This approach has its first appearances in the work of Maganani et al (1997) and Silin and Patzek (2006). The method looks for the largest ball inscribed in the pore space, touching the surface of the grains. The search is performed by creating centralized balls in every pore of the three-dimensional voxel image. As a result, the balls that are completely included in larger balls are removed. The developed computer code has a strong foundation in the works of Al-Kharusi (2008) and Dong (2007), especially in the latter, by the way he conceived the clustering step and the use of two values for radius of a discrete sphere.

2.1 Steps for pore-network extraction

The pore-network extraction using maximal balls methodology from a binary image of the porous medium consists of four steps:

1. Search for inscribed balls
2. Search for maximal balls
3. Clustering
4. Throat expansion

Figure 3 illustrates the network extraction showing the image acquisition in gray scale, binarization, search for inscribed and maximal balls, clustering and throat expansion (as covered in the next section).

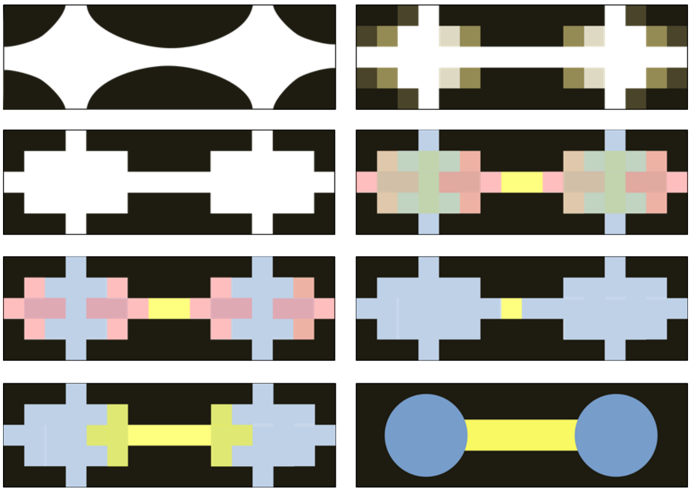

Figure 3 Steps in pore-network generation from original porous space to the network representation

2.2 Search for inscribed balls using euclidian distance transformation

The discrete ball as the name implies is a representation of this element in a discrete domain (a set of voxels). A sphere whose center is located in a particular voxel (i, j, k) with radius R is defined by the set of voxels:

$$\left\{(i,j,k);(i-c_i)^2+\left(j-c_j\right)^2+(k-c_k)^2\leq R^2\right\} \tag{2}$$

For the three dimensional domain, Figure 5 shows spheres with radii $\sqrt{2}$, 2 and $\sqrt{14}$. Dong used the concept of two radius values to define a discrete sphere: R_{min} and R_{max}. R_{max} is equivalent to the concept discrete sphere radius presented in equation (2), R_{min} will be the largest distance between the sphere center and one of its pore voxels. They present the property that any continuous sphere with radius r such that $R_{min} < r < R_{max}$, when discretized, will produce the same discrete sphere.

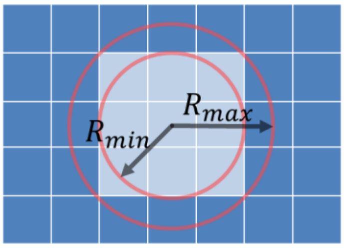

Figure 4 Representation of R_{min} and R_{max} of a discrete sphere

The first step of the method is to fill the pore space of the binarized image with discrete spheres. To do so, spheres will be create centered at each pore voxel. Thus, at the end of this stage there will be as many spheres as pore voxels in the image.

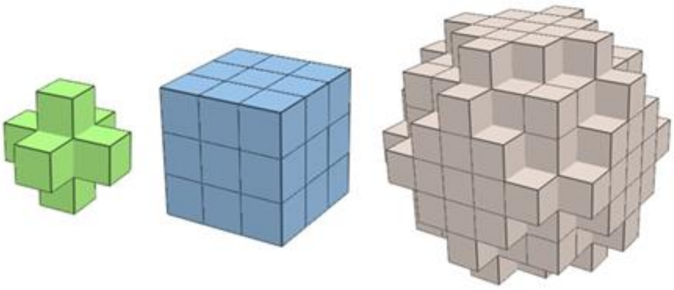

Figure 5 Discrete spheres at three dimensional domain

The radius of the sphere is as large as possible, so long as the ball has only voxels belonging to the pore space. This is accomplished with an euclidean distance transform of the binarized image. In image processing, the distance transformation (DT) consists of converting a binarized image into another image called distance map, where each element of the *foreground* has a value corresponding to the distance to the closest *background* element, which in this context means the shortest distance of a pore voxel to a grain voxel. This will result precisely in the inscribed discrete sphere radius centered in that particular voxel.

Saito and Toriwaki (1994) developed an optimized algorithm to the squared euclidean distance transformation (SEDT). The algorithm consists of an initial one-dimensional transformation on the image primary direction (x-axis). Considering a two-dimensional image P, the initialization step will generate a image g such that, for a given row j:

$$g(i,j) = \min\left\{ |i-x| ; 0 \le x < m \ and \ (x,j) \in P \right\} \tag{3}$$

This initialization can be achieved with a simple algorithm consisting of two labeling scans. At the end of this stage each will have the euclidean distance to the nearest voxel grain, but considering only the voxels from its line (j).

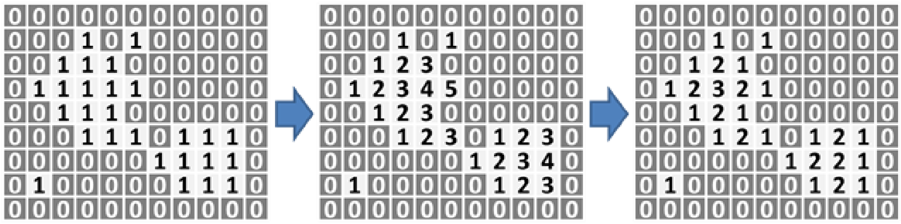

(a) (b) (c)

In the following steps, for each dimension it is performed a column to column process where the values obtained in the previous step are used to construct a set of parabolas, as shown in equation (4), where F represents a parabola for a given column of the image. The value found in the previous stage for position (i, j) is represented by $g(i, j)$.

$$F_{i,j}(y) = g(i,j)^2 + (y-j)^2 \tag{4}$$

The value for the second stage is computed from the inferior envelope extracted from the set of parabolas for each column:

$$h(i,j) = \min\left\{ g(i,j)^2 + (y-j)^2 \ ; 0 \le y \le n \right\} \tag{5}$$

In order to illustrate the process, Figure 6 and Figure 7 show the set of parabolas, the inferior envelope for column 4 and 9, and the obtained result.

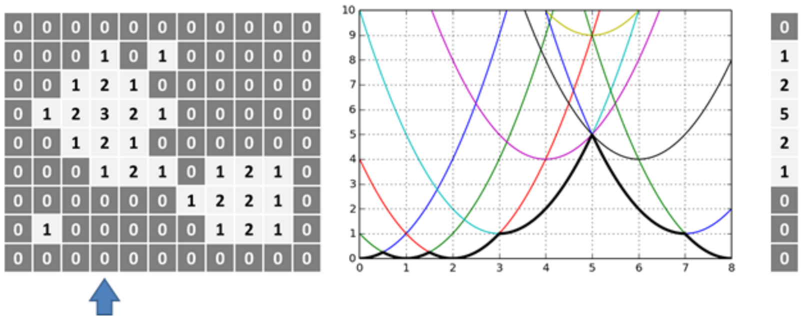

Figure 6 Set of parabolas, inferior envelope and result for column 4

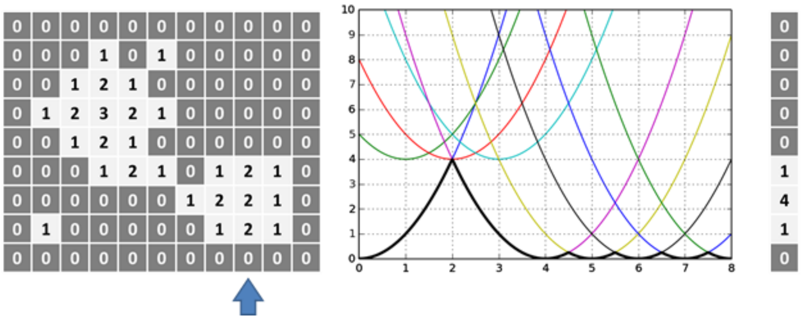

Figure 7 Set of parabolas, inferior envelope and result for column 9

For a third dimension, the same process will be applied, in such a way that the set of parabolas will be given by $F_{i,j,k} = h(i,j,k)^2 + (z-k)^2$. At the end, this algorithm will build a matrix where each element will represent a inscribed sphere on the binarized image. Its center is given by its position in the matrix, and the radius is given by its value.

2.3 Search for maximal balls (removal of inclusions)

The goal of finding inscribed discrete spheres in the pore space is to be able to represent it through these elements, thus some of the spheres become unnecessary since they are completely included within one or more larger spheres. The “removal of inclusions” step will give the least number of balls that together compose all the pore voxels of the image. This subset of inscribed spheres receives the name of maximal balls. In other words, a maximum ball is an inscribed sphere which has at least one pore voxel that does not belong to any other sphere. Figure 6 shows a set of inscribed balls found in a binarized image (a) and the corresponding maximal balls (b) for this case.

In order to identify inclusion, Dong (2007) and Al-Kharusi (2008) evaluate subsets of combinations of two inscribed spheres, using their radius and centers distance

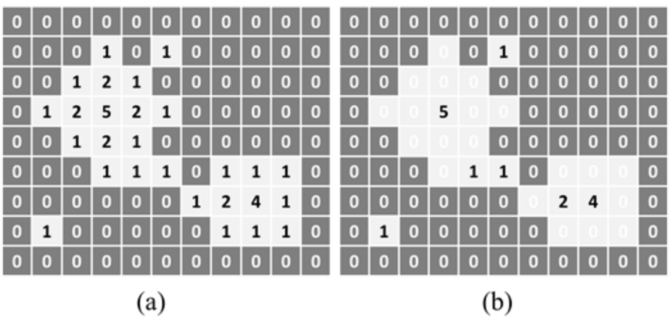

Figure 8 Maximal balls (b) as a subset of inscribed balls (a)

The test for inclusion of a given sphere *B* in another sphere *A* is positive in case:

$$\mathrm{dist}(C_A, C_B) \leq R_A - R_B \tag{6}$$

Figure 9 shows the final result for the maximal balls search in a porous space represented as gray colored voxels. The maximal balls voxels are represented in different colors.

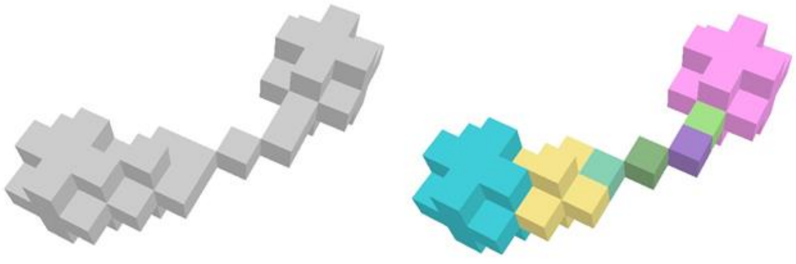

Figure 9 Maximal balls found in a simple three dimensional case

2.4 Clustering

Clustering is the first step to be held in the pores and throats identification process. Pores and throats are defined by grouping different sets of maximal balls. Clustering step therefore seeks to find and establish relationships between the intersecting or adjacent maximal balls. This will allow determining whether a sphere is part of a pore or throat according to criteria that will soon be presented.

A sphere A will intersect with another sphere B if:

$$dist\left(C_A, C_B\right) \leq R_{Amax} - R_{Bmax} \tag{7}$$

The methodology used for clustering is based on Dong design (2007), using the concept of family trees. Two new properties are assigned to the spheres: a generation number and a "family name". The largest spheres are treated as ancestors from first generation and give name to a family. This family name is passed on to the balls that intersect with it which will then be defined as a direct children and classified as generation 2. All spheres are then visited in this order, intersecting spheres are analyzed and the name of its family is passed along to those who have a younger generation or have not yet been visited. All spheres are classified as belonging to the pore formed by their respective ancestor. By the end of this stage, the spheres which have more than one family name will be classified as a throat, being the connection between the ancestors of each family.

To clarify this, take the example given in Figure 9, where seven maximal balls were found, each one represented by a different color. As shown in Figure 10 the bigger spheres with $R_{max}^2 = 2$ are identified as ancestors and generation 1. Therefore, their family names are passed alog to the adjacent spheres, which will have one generation higher than their parents.

At the end of the process one sphere is identified as having two ancestors, being classified as a throat that connects the ancestors of families 1 and 2, and two pores are identified containing three spheres each.

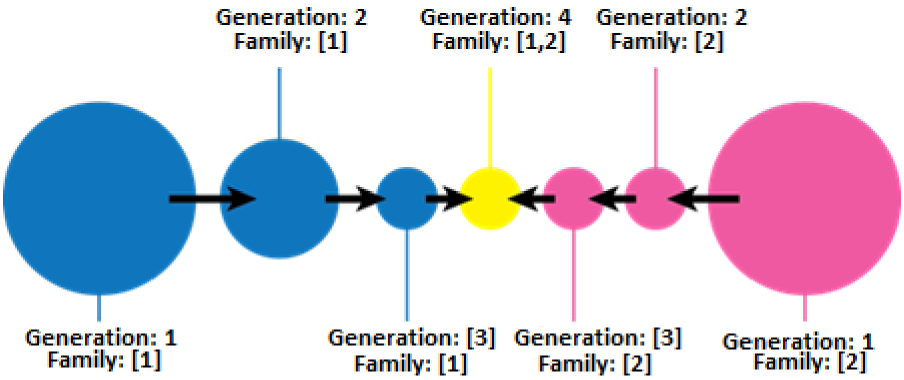

Figure 10 Clustering of example presented in Figure 9

2.5 Throat expansion

In order to represent the elongated apertures connecting pores, the throat in the example given in Figure 10 should not be represented as a single sphere. This sphere assigned as throat is called throat seed.

In order to capture the expected morphology of the throat it is necessary to identify the spheres that compose the way between the throat seed and the family ancestors. This step is called throat expansion and will be responsible for the final segmentation of the porous space, which means differentiating pores and throats bodies.

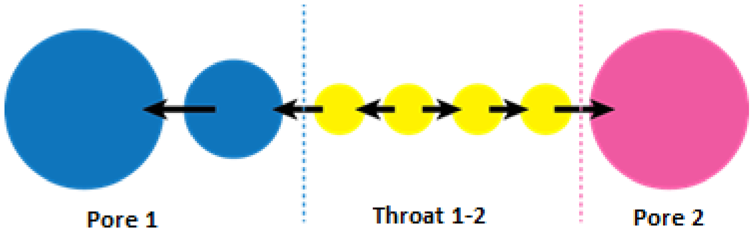

Figure 11 Throat expansion from example presented in Figure 9

Mandatorily, ancestral spheres will be part of pores and the throat seed which already have the fundamental characteristic of a throat (connected with more than one ancestral sphere) will be part of the throat. All spheres found in the path between this seed and their ancestors are candidates for classification, where part of them will constitute the pore volume and the rest of the throat. The identification of this interface can perhaps be detected in a visual analysis, but it is necessary to adopt a choice criterion in order to implement a computational algorithm to perform this task. The chosen criterion is called the expansion factor E_f. It is the ratio between the R_{min} of the sphere being analyzed and the difference between the ancestral sphere and throat radii. Thus, certain sphere of radius will be classified as throat if its expansion factor is less than a certain maximum amount stipulated:

$$\frac{R_{i,min}}{R_{a,min} - R_{g.min}} < E_{fmax} \tag{8}$$

In this work the value used for E_f is 0.7 based on Dong, (2007) and Silva (2012).

3 PETROPHYSICAL PROPERTIES PREDICTION

In order to use the network to perform predictions of petrophysical properties related to transport it is necessary to develop a mathematical model to simulate fluid flow through pore and throats. The model uses the following hypothesis:

- Fluid is newtonian and incompressible;
- Flow is in steady state;
- Fluid is composed of a single pahse and have homogeneous properties;
- Flow is in laminar regime;
- Pressures in boundary pores are known.

The goal is to obtain an equation system for pore pressures, allowing the calculation of flow from one pore to another. This will be achieved by using Poiseulle equation for duct flow. The starting point to model is the evaluation of mass conservation equation for each pore in the network. Considering the hypothesis above, the equation for a pore *i* that connects to *j* pores could be written as:

$$\sum_j Q_{ij} = 0 \tag{9}$$

The pore network can be decomposed in several pore-throat-pore systems according to Figure 13, this sytem is composed by two hemispheres belonging to the pair of pores and the cylindrical throat. Flow from one pore to another is calculated using Poiseulle equation. This equation relates flow Q to the pressure difference between the pores ΔP.over their distance l and a hydraulic conductance γ.

$$Q = -\gamma \frac{\Delta P}{l} \tag{10}$$

Porous structures will be approximated to prismatic elements with constant cross-section shapes (Valvatne, 2004), (Øren, et al., 1998), (Patzek & Silin, 2001) that can assume either circular, square, or triangular figures, which will be chosen to the one that has equivalent two-dimensional shape factor ($G = A/P^2$, where A stands for the shape area, and P for its perimeter) compared to the three-dimensional shape factor from the original geometry($G = VL/A_s^2$, where V corresponds to its volume, A_s to the superficial L to the length in flow direction). This transformation is illustrated in Figure 12.

Hydraulic conductance can be expressed in a generic way using the shape factor concept, where A stands for cross-section area of the porous body (pore or throat) in the flow direction, and α is a parameter that will assume the value of $1/2$ for circular, $3/5$ for square and 0.5623 for triangular sections:

$$\gamma = \alpha \frac{A^2 G}{\mu} \tag{11}$$

So hydraulic conductance for the pore-throat-pore system can be written as:

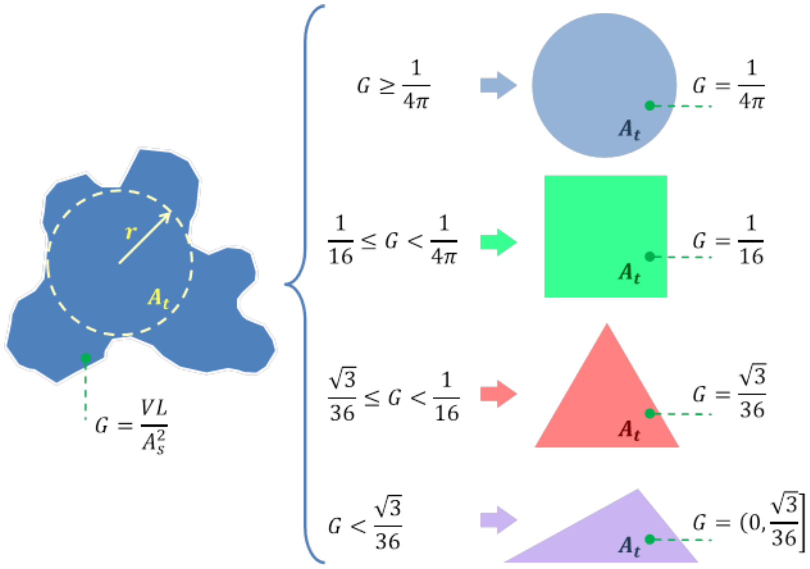

Figure 12 Approximation of the original porous structure to a prism with constant cross section shape

$$\gamma_i = \alpha_i \frac{A_i G_i}{\mu} \quad \gamma_j = \alpha_j \frac{A_j G_j}{\mu} \quad \gamma_g = \alpha_g \frac{A_g G_g}{\mu} \tag{12}$$

Equation (10) can be written using the concept of hydraulic resistance:

$$Q = -\Omega_{eq}^{-1} \Delta P \tag{13}$$

Where equivalent resistance is defined by:

$$\Omega_{eq}^{-1} = \frac{\gamma_i}{l_i} + \frac{\gamma_{i,j}^g}{l_{i,j}^g} + \frac{\gamma_j}{l_j} \tag{14}$$

Applying equation (14) in mass conservation equation:

$$\sum_j -\Omega_{i,j}^{-1} \Delta P_{i,j} = 0 \tag{15}$$

Evaluating this for each pore of the network containing *n* pores, a linear equation system can be assembled as in equation (16). Assuming pressure in the boundary pores are known, the system has a unique solution.

$$\left[\Omega^{-1}\right]_{n\times n} \left[\Delta P\right]_{n\times 1} = \left[0\right]_{n\times 1} \tag{16}$$

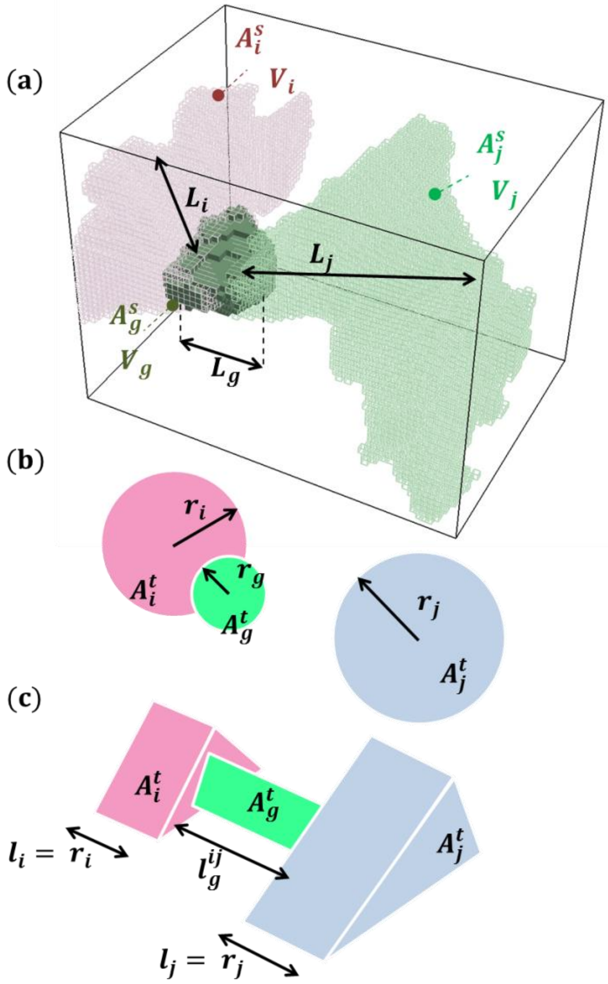

Figure 13 Pore-throat-pore system

4 RESULTS AND DISCUSSION

4.1 METHODOLOGY

All tomographic images were acquired using micro CT Bruker Skyscan 1173. The acquisition of each 3D reconstructed image felt the following procedure:

1. Preheating the x-ray source for 15 minutes;
2. Calibration of flat field panel for black and white conditions;
3. Positioning of plug sample;
4. Acquisition parameter (brass filter1, 20 µm resolution2, medium of 4 samples for each images, 360º rotation, 0,2º rotation for image, 5 pixels horizontal random movement, energy of 130 kV and current of 61 µA);
5. Reconstruction parameters (histogram definitions, bean hardening, ring artefact correction and 360º) generating a greyscale 3D image – for reconstruction a GPU based algorithm was used;

6. Binarizaion (see details below) of greyscale 3D image generating a black and white 3D image;

To improve image contrast on higher density samples (travertine and sandstone) during acquisition procedures a physical x-ray filter was development and applied in combination with Brass filter. It works restricting the passage of photons of lower energy more intensely than the highest energy photons. Considering that, the maximum power available by the equipment is 130 KV the chosen material to create the filter was stainless steel. Calculated outcomes are shown in Figure 1.

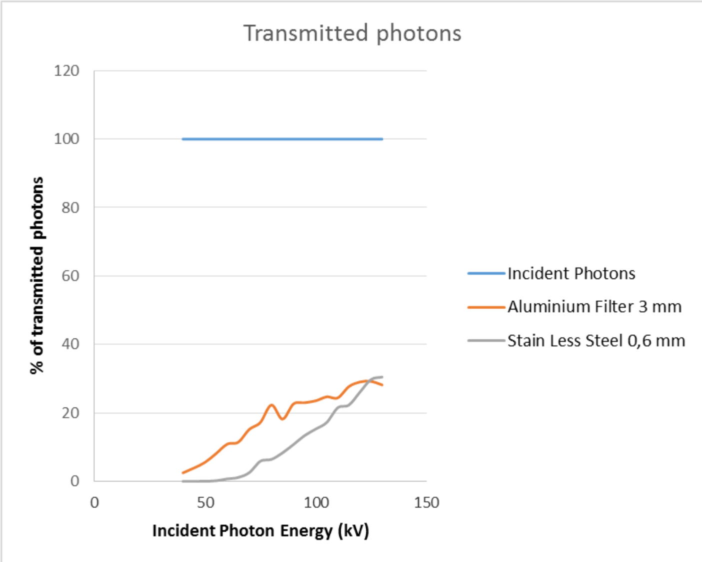

Figure 14 Calculated comparison of transmitted photons after application of different metallic filters.

The application of the filter resulted in a significant increase contrast, especially in the higher density samples such as travertine sandstones, which are denser than the Tufa and Stromatolite.

4.2 Binarization procedures

Binarization or threshold procedure is the main step where the limits of matrix and pore space is defined. For the reason that tomographic images have a well-known artefact, known as partial volume effect, this differentiation is not immediate. For heterogeneous samples, like carbonates, where one can find small high density structures inside low density structures or the contrary this effect can become very significant and lead to systemic imprecise measurements.

In order to increase accuracy of this procedure and obtain results for heterogeneous carbonate rocks the implementation of different logical filters were verified. A variety of algorithms like automatic threshold as Otsu's method and Ridler's iterative method were tested, however the best results were obtained for an in house customized procedure. The procedure is a combination of unsharp masking a global threshold.

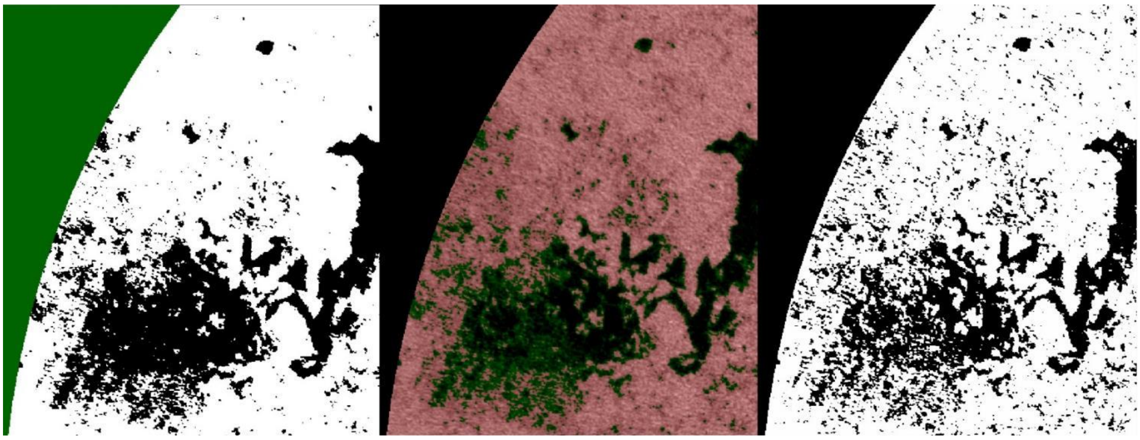

Figure 15 Detail in image presenting the comparison of different filters applied to travertine binarization in resolution of 19.9 micrometers.

In Figure 15, it may be noted that the original image to the center were obtained two different segmentations:

- The segmentation shown in right position was obtained by a global threshold, which fails in identification of small rock segments distributed in also large pores and to identify small pores embedded in dense rocks parts.
- The segmentation shown in left position it was obtained by sequentially applying unsharp masking filter following global threshold and efficiently identify the structures of the left ignored by the fist method.

Figure 16 shows the resulting porosity calculations after the application of different binarization procedures. Better differentiation of pore and matrix were obtained with a unsharpenig 3D radius 2 and threshold 65 (0 to 255).

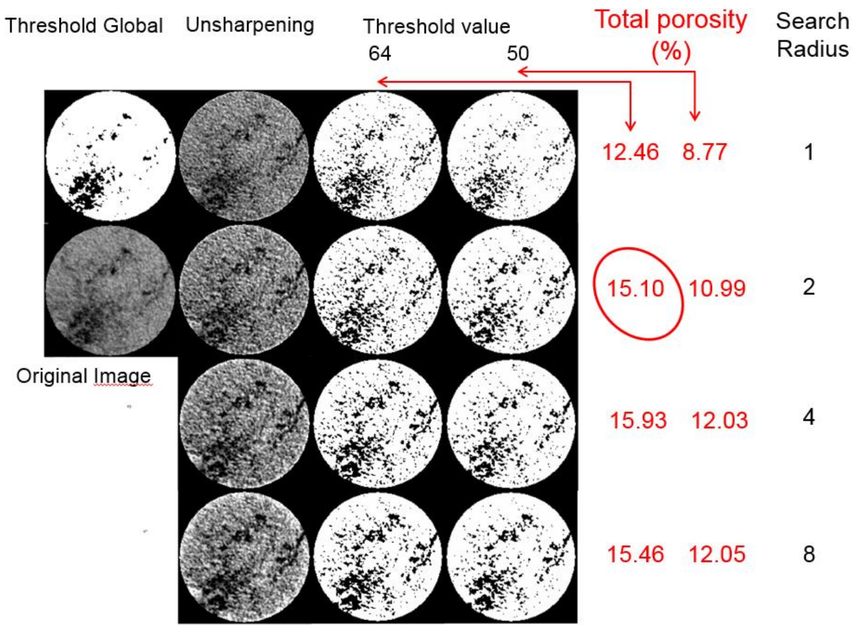

Figure 16 porosity results for different binarization procedures.

4.3 Laboratory porosity and permeability measurements

All porosity and permeability analyses were performed by Coretest Systems AP- 608 Automated Permeameter-Porosimeter. In this equipment, permeability measurements are made using an unsteady state pressure decay technique. Porosity and pore volume are measured using Boyle´s law technique.

The acquisition of each parameter felt the following procedure:

- Keeping samples on Laboratory oven for 12 hours;
- Certifying sample integrity3 and cylinder format;
- Helium pressure verification;
- Adjust coreholder to sample height;
- Reference and internal volume calibration;
- Load sample on coreholder;
- Complete three measurements for each sample;

4.4 Extracted networks for Berea Stone and Travertine

Two images were used for characterization, one from Berea stone acquired with a resolution of 9.9 µm and one from a travertine sample (pre-salt analogue) acquired with a resolution of 18 µm. The Berea image resolution was limited to this value because higher resolutions for required a subsample extraction from the plug, due to the necessary proximity from the sample and the X-Ray source, which was impossible at the moment. While for Travertine, a single resolution value choice is a complex issue due to the large range of porous structures geometric scale. The value of 18 µm were used in order to capture the bigger porous structures existing in the sample which importance to permeability were expected to be higher.

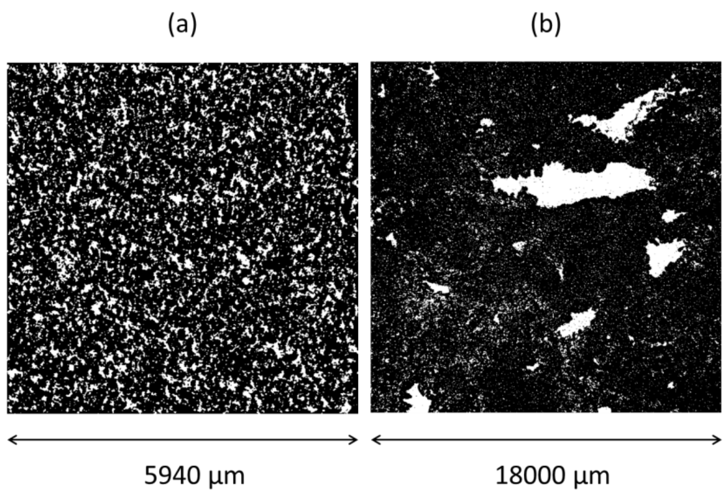

Figure 17 Sections from the binary image from the ROI of Berea sndstone (a) and Travertine (b)

A region of interest (ROI) was used in both images to extract the pore-networks. ROI for Berea stone had 600^3 voxels, and for Travertine 1000^3 voxels were used. The number of pores and throats found for each pore-network is presented in Table 1.

Table 1 Number of pores and throats from the extracted pore-network for Berea sandstone and Travertine

	Number of pores	Number of throats
Berea Stone	78340	45762
Travertine	4104088	477788

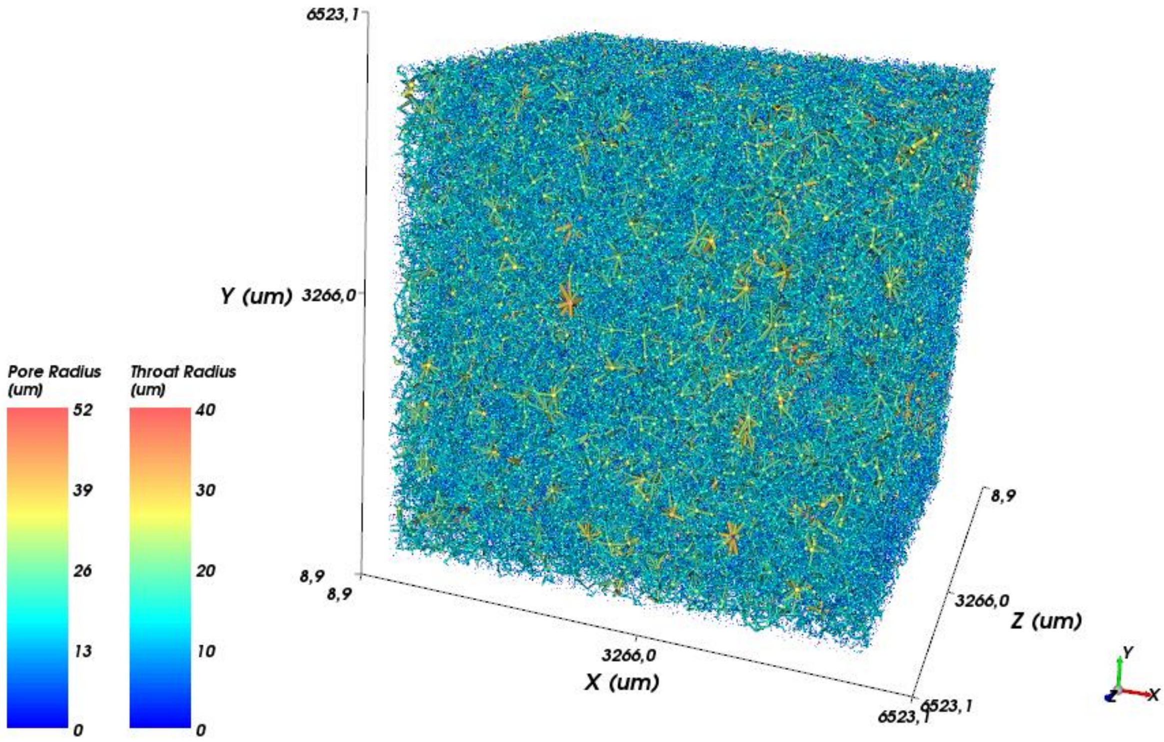

Figure 18 Visualization of Berea sandstone pore-network showing pore and throat radius.

4.5 Porosity and absolute permeability

Permeability and effective porosity were experimentally obtained for Berea and Travertine, presented in Table 2.

Table 2 Porosity and absolute permeability of samples measured in laboratory

	Porosity (%)	K_{air} (mD)	K_{klink} (mD)
Berea stone	17.978	373.828	368.571
Travertine	14.86	8.19	8.88

Table 3 Porosity and absolute permeability obtained from pore-network model

	Porosity (%)	Permeability (mD)
Berea stone	20.03	323.08
Travertine	13.75	2.93

4.6 Conclusions

Permeability obtained from pore-network simulation for Berea sandstone presented the same order of magnitude, however lower than laboratory measurements. There are indications that results for this case could have a better agreement if higher resolution was used during image acquisition. Dong (2007, p. 161) suggests that a high number of disconnected pores (pores with zero coordination number which corresponds to the number of connections a pore have) indicated that insufficient resolution was used, meaning that porous structures smaller than 9.9 μm existed in the sample. These porous paths that were not captured could be responsible for the higher permeability values found in experimental data. A solution to that is to obtain a subsample from the original plug and acquire an image with higher resolution.

Travertine sample is an example of a very complicated sample, as it is highly heterogeneous and present very different scales of porous structures. Results from the model shows permeability of 2.93 mD while measured in laboratory samples revealed 8.88 mD. In this case a resolution of 18 μm was chosen because it was expected that bigger pores found in the sample would have greater importance in fluid transmissibility. However it is known that in rocks like carbonates these large porous structures are very often supposed to be disconnected, which would result in high storage capability and low permeability. But often this is not what happens as these large structures are connected by smaller pores, which would not be captured by this resolution. In cases like these, it is proposed to work with not one but several scales from the same sample (Mantovani, 2013). In order to achieve this, subsamples are extracted and each image is acquired with a different resolution. Different pore-networks are extracted from each image, and on a final stage a multi-sale pore-network is generated stochastically in order to contemplate the different scales of these rocks. This kind of analysis could be the solution to achieve closer results from the model and experimental data.

REFERENCES

Al-Kharusi, A. S. & Blunt, M. J., 2008. Multiphase flow predictions from carbonate pore space images using extracted network models. *Water resources research,* 44(6).

Benzi, R., Succi, S. & Vergassola, M., 1992. The lattice Boltzmann equation: theory and applications. *Physics Reports,* 222(3), pp. 145-197.

Chen, S. & Doolen, G. D., 1998. Lattice Boltzmann method for fluid flows. *Annual review of fluid mechanics,* 30(1), pp. 329-364.

Cunha, A. et al., 2012. Determinaçã}ao de propriedades petrofísicas de rochas via simulaçãao. Um caminho interdisciplinar. *Revista Brasileira de Ensino de Física,* 34(4), p. 4315.

Dong, H., 2007. *Pore-Scale characterization of carbonate rocks.* s.l.:s.n.

Magnani, F. S., Zhirong, L., Philippi, P. C. & Fernandes, C. P., 1997. Extraction of 3D Pore Network and Prediction of Permeability for Reservoir Rocks. *XIV Brazilian Congress of Mechanical Engineering.*

Mantovani, I., 2013. Microtomografia e Nanotomografia de Raios X aplicada à caracterização multiescalar de sistemas porosos carbonáticos.

Øren, P.-E. & Bakke, S., 2002. Process based reconstruction of sandstones and prediction of transport properties. *Transport in Porous Media,* 46(2-3), pp. 311-343.

Øren, P.-E. & Bakke, S., 2003. Reconstruction of Berea sandstone and pore-scale modelling of wettability effects. *Journal of Petroleum Science and Engineering,* 39(3), pp. 177-199.

Øren, P.-E., Bakke, S., Arntzen, O. J. & others, 1998. Extending predictive capabilities to network models. *SPE Journal,* 3(04), pp. 324-336.

Patzek, T. & Silin, D., 2001. Shape factor and hydraulic conductance in noncircular capillaries: I. One-phase creeping flow. *Journal of colloid and interface science,* 236(2), pp. 295-304.

Rothman, D. H. & Zaleski, S., 1994. Lattice-gas models of phase separation: interfaces, phase transitions, and multiphase flow. *Reviews of Modern Physics,* 66(4), p. 1417.

Saito, T. & Toriwaki, J.-I., 1994. New algorithms for euclidean distance transformation of an n-dimensional digitized picture with applications. *Pattern recognition,* 27(11), pp. 1551-1565.

Silin, D. & Patzek, T., 2006. Pore space morphology analysis using maximal inscribed spheres. *Physica A: Statistical Mechanics and its Applications,* 371(2), pp. 336-360.

Silva, A. F. B. & others, 2012. Caracterizaçãoo do espaço poroso em rochas por esferas máximas exatas.

Valvatne, P. H., 2004. *Predictive pore-scale modelling of multiphase flow,* s.l.: s.n.